



Direct-ink-write cross-linkable bottlebrush block copolymers for on-the-fly control of structural color

Sanghyun Jeon^{a,1}, Yash Laxman Kamble^{b,1}, Haisu Kang^{b,1}, Jiachun Shi^{b,1}, Matthew A. Wade^b, Bijal B. Patel^b, Tianyuan Pan^{a,c}, Simon A. Rogers^{b,c,2}, Charles E. Sing^{b,c,2}, Damien Guironnet^{b,c,d,2}, and Ying Diao^{b,c,2}

Edited by Joseph DeSimone, Stanford University, Stanford, CA; received August 8, 2023; accepted January 16, 2024

Additive manufacturing capable of controlling and dynamically modulating structures down to the nanoscopic scale remains challenging. By marrying additive manufacturing with self-assembly, we develop a UV (ultra-violet)-assisted direct ink write approach for on-the-fly modulation of structural color by programming the assembly kinetics through photo-cross-linking. We design a photo-cross-linkable bottlebrush block copolymer solution as a printing ink that exhibits vibrant structural color (i.e., photonic properties) due to the nanoscopic lamellar structures formed post extrusion. By dynamically modulating UV-light irradiance during printing, we can program the color of the printed material to access a broad spectrum of visible light with a single ink while also creating color gradients not previously possible. We unveil the mechanism of this approach using a combination of coarse-grained simulations, rheological measurements, and structural characterizations. Central to the assembly mechanism is the matching of the cross-linking timescale with the assembly timescale, which leads to kinetic trapping of the assembly process that evolves structural color from blue to red driven by solvent evaporation. This strategy of integrating cross-linking chemistry and out-of-equilibrium processing opens an avenue for spatiotemporal control of self-assembled nanostructures during additive manufacturing.

bottlebrush block copolymer | self-assembly | additive manufacturing | photonics | structural color

The biological world provides exquisite examples of how simultaneous control over molecular composition and long-range macroscopic order gives rise to material properties that seem unique to living organisms. For example, the phenomenon of structural color is found in a variety of animals, including birds (1), butterflies (2), fish (3), insects (4), and chameleons (5). This coloration property arises from the periodic ordering of domains with different refractive indices on the nanometer length scale. Structural color is a compelling alternative to synthetic color because it can be eco-friendly in contrast to the environmentally polluting synthetic dyes (6). Further, structural color can exhibit high brilliance and dynamic properties that are challenging to attain through synthetic routes (7, 8). These advantages have motivated extensive efforts to achieve structural color in synthetic materials (7–11). While top-down lithographic approaches have been successful at producing precise periodic structures (12, 13), they require sophisticated and costly processing steps to achieve nanoscopic feature size, which limits scalability and broad applicability. Bottom-up self-assembly methods of creating nanostructured materials such as blue-phase or chiral liquid crystals (14–16), colloidal nanoparticles (17–22), and block copolymers (23–26) have been explored to address these limitations. Among these materials, block copolymers show great promise in mimicking biological structural color as it can access a wide range of nanoscale morphologies encompassing lamellar, cylindrical, bicontinuous, and spherical morphologies. (11, 27–41). However, achieving visible-range coloration is non-trivial due to chain entanglement and sluggish assembly kinetics, limiting their ability to access domain sizes large enough to reflect visible light (42, 43). To overcome this challenge, domain swelling strategies have been developed (24, 44, 45), but pose challenges in terms of environmental stability.

Bottlebrush block copolymers (BBCP) comprising densely grafted side chains attached to a common backbone represent a promising alternative to linear block copolymers for achieving visible-range structural coloration (10, 43, 46–51). The steric repulsion between dense side chains leads to extended cylindrical conformations and suppressed chain entanglement, which facilitate rapid self-assembly into ordered nanostructures with large domain sizes (43, 46, 52-54). The facile production of photonic crystals using BBCP opens up a wide range of potential applications, such as in the production of photonic resins (42), photonic pigments (55–57), stress-responsive photonic structures (58, 59), and 3D printed photonic structures (23, 60).

Significance

Structural color, drawing inspiration from nature, offers sustainable, eco-friendly, and dynamic coloration properties that are challenging to achieve with traditional synthetic dyes. Bottlebrush block copolymer has garnered significant attention due to its rapid assembly characteristics into plethora nanoscale morphologies with large domain spacing conducive to vibrant photonic properties. In this work, we demonstrated that integrating cross-linking chemistry with out-of-equilibrium processing based on additive manufacturing allows for dynamic control of structural color across the visible light spectrum and creates color gradients using a single ink. This approach demonstrates the power of non-equilibrium processing in dynamically modulating self-assembled structures and their functional properties during additive manufacturing.

Author contributions: S.J., S.A.R., C.E.S., D.G., and Y.D. designed research; S.J., Y.L.K., H.K., J.S., M.A.W., B.B.P., and T.P. performed research; Y.L.K. and H.K. contributed new reagents/analytic tools; S.J., Y.L.K., H.K., J.S., M.A.W., and B.B.P. analyzed data; and S.J., Y.L.K., H.K., J.S., S.A.R., C.E.S., D.G., and Y.D. wrote the paper.

The authors declare no competing interest.

This article is a PNAS Direct Submission.

Copyright © 2024 the Author(s). Published by PNAS. This article is distributed under Creative Commons Attribution-NonCommercial-NoDerivatives License 4.0

¹S.J., Y.L.K., H.K., and J.S. contributed equally to this work.

²To whom correspondence may be addressed. Email: sarogers@illinois.edu, cesing@illinois.edu, guironne@ illinois.edu, or yingdiao@illinois.edu.

This article contains supporting information online at https://www.pnas.org/lookup/suppl/doi:10.1073/pnas. 2313617121/-/DCSupplemental.

Published February 20, 2024.

Recently, our team developed an approach that combines additive manufacturing with BBCP self-assembly to attain control of printed structures down to the nanoscopic scale (60). We showed that a single BBCP ink can produce multicolored prints by modulating simple printing parameters (such as the speed and substrate temperature) of a custom-made DIW (direct ink write) 3D (Threedimensional) printing (60, 61). This innovation leverages a kinetic trapping mechanism whereby evaporation-driven assembly was arrested before reaching the equilibrium structure through rapid solvent evaporation (60, 62). This approach presents an effective strategy to modulate structural color of a single ink but is limited in achieving "on-the-fly" control of color during printing. This is because temperature and printing speed are not ideal "knobs" for tuning assembly—temperature cannot be changed rapidly and is difficult to localize, while printing speed is coupled with line profiles and thus structural color cannot be adjusted independently.

In this work, we achieve on-the-fly modulation of structural color during printing by combining a UV-assisted DIW 3D printer with c-BBCP (cross-linkable BBCP) chemistry. A key innovation is to realize dynamic control of assembly kinetics through programming the rate of photo-cross-linking, which serves to kinetically arrest assembly and lock in desired structural color on-the-fly, or as we print. We then validate two key aspects of this hypothesis by combined coarse-grained simulations, rheological characterizations, and experimental structural analysis. First, using the "implicit side-chain" (ISC) model developed by our team (62-66), we elucidate an evaporation-driven assembly pathway whereby the structural color evolves from blue to red due to backbone extension. This inference is affirmed by scanning electron microscopy (SEM) and ultra-violet visible (UV-Vis) spectroscopy. Second, by rheology and in situ imaging, we show that the cross-linking timescale matches with the evaporation-driven assembly timescale, supporting the idea that assembly is arrested by cross-linking during evaporation-driven structural evolution. Enabled by this mechanistic understanding, we program the temporal profile of UV irradiance to demonstrate modulation of structural color on the fly as to access much of the visible spectrum and to create color gradients using a single ink material.

Results and Discussion

Our approach to on-the-fly printing of BBCP materials with structural color is built on the co-design of both molecular synthesis and printing process; we show how innovations in each combine to give unprecedented control over structural color. We subsequently investigated the physicochemical foundation for this effect to provide design principles for dynamically controlling assembly through additive manufacturing. We further demonstrate how our approach enables on-the-fly direct ink writing of vibrant and tunable structural color.

Synthesis of Cross-Linkable BBCP. We developed a postpolymerization modification technique to introduce cross-linking groups at the tips of the PLA brushes of PS-b-PLA (polystyrene-bpolylactide) c-BBCP. Post-polymerization modification is a wellestablished methodology for the introduction of functionalized groups in linear polymers (67–78). However, the post-polymerization modification of bottlebrush polymers presents additional complexity because of the risk of alteration of the original bottlebrush architecture, with PLA being especially susceptible to transesterification and thus broadening of the molecular weight distribution (MWD) (79). Furthermore, we recently demonstrated that Gel Permeation Chromatography (GPC), the workhorse

characterization technique for polymers, is not effective at assessing the alteration of PLA segments along the bottlebrush polymer since the MWD of the bottlebrush polymer is primarily impacted by the MWD of the backbone and not of the side chains (80). Therefore, we needed to identify a post-polymerization functionalization reaction to address these limitations and with the scope of employing thiolene click chemistry to achieve the UV-assisted cross-linking of c-BBCP (81).

We identified an alcohol-isocyanate reaction catalyzed by tin-dibutyl diacetate as a simple reaction to introduce an allyl group at the tips of PLA brushes (82). To demonstrate the success of the post-polymerization reaction and the absence of degradation of the original bottlebrush architecture, we first set out to develop the methodology with a UV-active 1-naphthyl isocyanate and homo-PLA bottlebrush polymers (Fig. 1A). By selecting a wavelength (266 nm) for which the naphthyl group has a strong absorption and the PLA is mostly transparent, we were able to monitor the extent of functionalization of the bottlebrush polymers using a combination of the UV detector of the GPC and ¹H NMR spectroscopy. By monitoring the gain in intensity of the bottlebrush signal as a function of time in the UV-GPC traces (using PS as an internal standard) (Fig. 1B) and assessing the mole fraction of naphthyl groups present in the polymer by NMR, we identified a reaction condition that resulted in >95% of the PLA tips of the BB being functionalized in absence of any degradation of the architecture. The absence of degradation is evident from the MWD signal retaining the same shape throughout the reaction along with the absence of low molecular weight fractions in the GPC traces.

We then implemented this post polymerization modification methodology to introduce allyl functionalities on the PLA side chain ends in the BBCP $PS_{200}^{4.5k}$ -b- $PLA_{236}^{4.8k}$ (Fig. 1*C*). The MWD of the c-BBCP remained unchanged through the post-polymerization reaction (Fig. 1D) and the integration of the allyl protons in the NMR spectrum suggested that >75% of the PLA brushes were functionalized. The reaction yielded ~20 g of functionalized polymers as highlighted in Fig. 1E. The allyl end-capped PLA side chains of the c-BBCP will undergo UV-triggered thiol-ene reaction in the presence of a thiol-functionalized cross-linker and a photo initiator as discussed in the later sections. The unsaturation present in poly(norbornene) backbone of the c-BBCP can also undergo possible thiol-ene reaction but the relative rates of this reaction as compared to allyl end-capped side chains is slower (81, 83–85). Thus, cross-linking of our c-BBCP system primarily occurs due to the presence of allyl groups on the side chain ends. Further synthetic details and characterization can be found in SI Appendix, Figs. S1-S8, and supplementary discussion in SI Appendix, section S1.

Establishing a Platform for UV-Assisted DIW 3D Printing. In parallel with designing cross-linking chemistries, we develop an additive manufacturing approach to achieve spatiotemporal control of photonic structure via modulating UV-triggered cross-linking during printing. To achieve this goal, two technical challenges needed to be overcome. First, the material dispensing, motion control, and UV light irradiation systems should be synchronized. Second, the cross-linking rate should be tunable by varying the UV light irradiance to match with the evaporation-driven assembly timescale (this criterion is discussed in depth later). To this end, we custom designed a UV-assisted DIW 3D printer based on our previously reported soft- and hard-ware framework PolyChemPrint (60, 61). We fabricated a printhead with suspended UV light guide Spot UV Curing system (OmniCure S2000, Excelitas) to

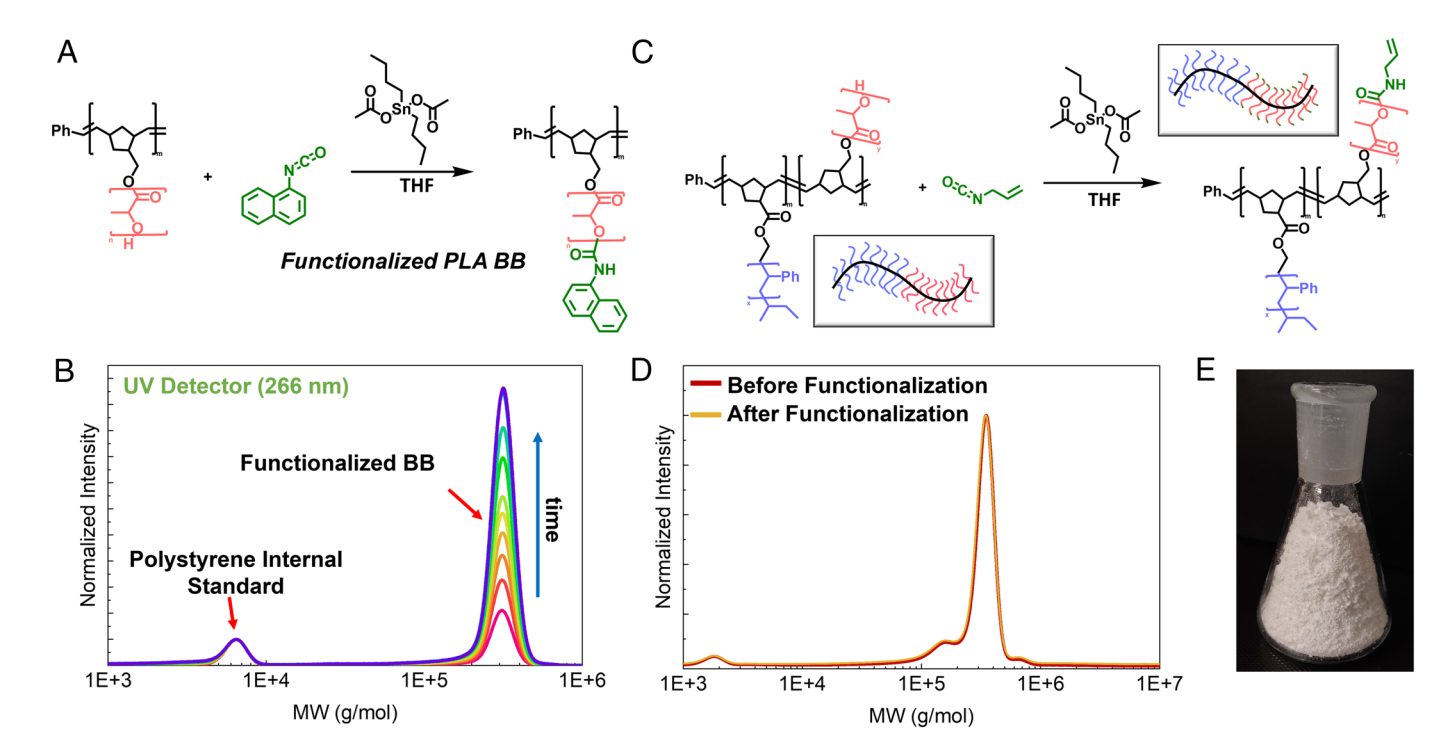


Fig. 1. Synthesis of the PS-b-PLA c-BBCP. (A) Reaction scheme for the functionalization of homo-PLA bottlebrush polymers with UV active end group using alcohol-isocyanate coupling reaction, (B) UV-GPC traces of the functionalized PLA bottlebrush polymer showing no change in bottlebrush polymer architecture (Internal Standard: 6 kg/mol PS; GPC data is evaluated using conventional calibration with respect to PS standards), (C) Reaction scheme for the functionalization of PS-b-PLA c-BBCP with cross-linkable allyl functionalities, (D) RI-GPC traces of the PS-b-PLA BBCP before and after functionalization (GPC data is evaluated using conventional calibration with respect to PS standards), (E) Image of dried functionalized BBCP as-synthesized at gram scales (~20 g).

directly illuminate UV light at the tip of a pneumatic dispenser (Fig. 2A). We further modified the PolyChemPrint software to develop PolyChemPrint3_UV that allows for programmable onthe-fly control of UV light on/off and irradiance during material dispensing (86). The UV lamp system offers the capability to adjust the UV light irradiance from 2 mW/cm² to 200 mW/cm². Additionally, by incorporating the UV light attenuator head, the range can be further tuned down to as low as 22 μW/cm², allowing us to widely tune cross-linking rates over orders of magnitude. The hardware and software framework thus offers on-the-fly modification of printing speed, applied pressure, and irradiated UV light at the same time, enabling precise cross-linking control over self-assembling c-BBCP solutions (Fig. 2B). A camera image of the hardware and details of the printer head design are shown in SI Appendix, Fig. S9 in SI Appendix, section S2.

On-the-Fly Tuning of c-BBCP Structural Color Using UV-Assisted DIW 3D Printing. The cross-linkable ink for UV-assisted DIW 3D printing comprises a concentrated c-BBCP toluene solution (250 mg/mL), a pentaerythritol tetrakis(3-mercaptopropionate) (PETMP) cross-linker and 2,2-dimethoxy-2-phenyl acetophenone photo-initiator (Fig. 3A). The solution concentration and printing conditions such as pressure and printing speed were optimized to ensure print fidelity and to prevent clogging or excessive ink spreading on the substrate (details shown in SI Appendix, Fig. S10 and supplementary discussion in SI Appendix, section S2). During the printing process, we observed a rapid visible color progression from blue to orange induced by the evaporation-driven selfassembly of c-BBCP (60, 62), which was captured by two cameras mounted at normal and 45° angles (SI Appendix, Fig. S11). Using intense UV light having irradiance in the range of 2 mW/cm² to 200 mW/cm² as produced by the OmniCure S2000 UV-curing system led to either rapid clogging of the printing tip or printing of a single blue color that was insensitive to the UV light irradiance. However, by substantially attenuating the irradiance of UV to a lower range (0 to 411 μ W/cm²), we were able to fine tune the structural color from orange to deep blue when the UV irradiance was increased from 0 to 411 μ W/cm² (Fig. 3B). As we shall show later, without attenuating the UV light, the cross-linking timescale is too short compared to the assembly timescale, preventing us from tuning structural color during printing.

We quantified this structural color shift by measuring the diffuse reflection spectra using UV-Visible spectroscopy with an integrating

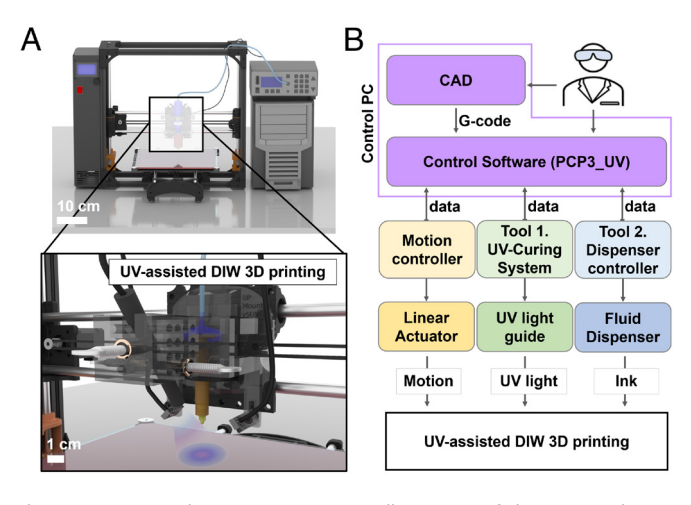


Fig. 2. UV-assisted DIW 3D printer. (A) Illustration of the printer design, featuring a custom-built pneumatic ink dispenser and a UV curing system for post-extrusion photo-cross-linking. (B) Developed PolyChemPrint3_UV (PCP3_UV) software framework that centrally controls and synchronizes the commercial 3D printer motion controller with custom-built UV curing system and ink dispenser.

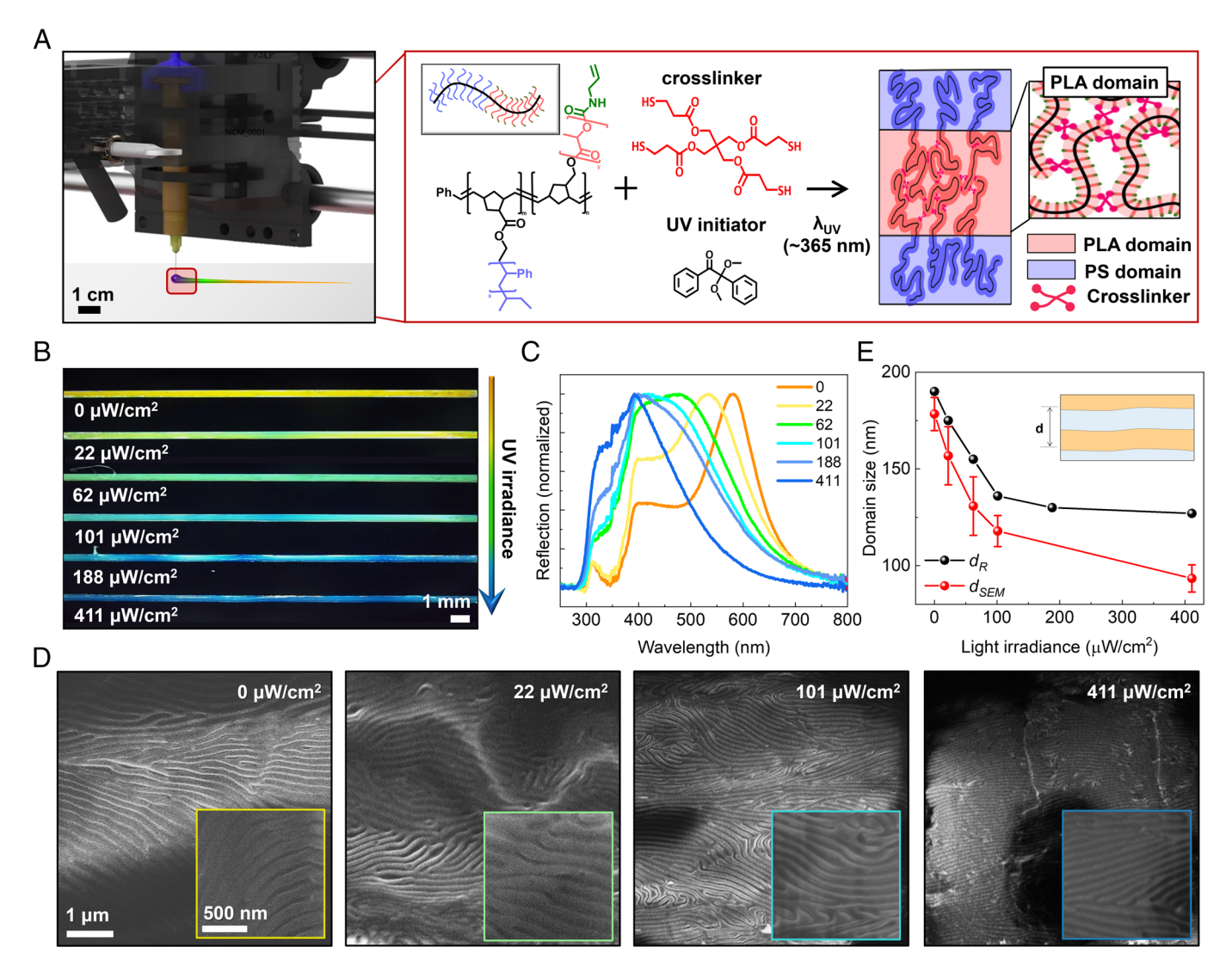


Fig. 3. On-the-fly tuning of structural color through UV cross-linking. (*A*) Schematic of UV-assisted DIW 3D printing process with the c-BBCP ink and the cross-linking reaction scheme. (*B*) The photograph depicts printed lines under varying levels of UV light irradiance during printing: 0, 22, 62, 101, 188, and 411 μ W/cm²; the image was captured using an upright optical microscope with diffusive ring lights. (*C*) The diffuse reflection spectra of each printed line under the varying UV irradiance (0, 22, 62, 101, 188, and 411 μ W/cm²). During measurement, the top surface of the lines faced the incident light, as this is the primary area where light reflection predominantly occurs. (*D*) Cross-sectional SEM images of printed lines under UV light irradiance of 0, 22, 101, and 411 μ W/cm². The *Inset* images are magnified SEM images for each sample, color coded based on the actual structural color of the structure (bright: PLA). (*E*) The estimated domain size calculated from the reflection peak maximum (d_R) and measured by SEM (d_{SEW}) as a function of UV light irradiance.

sphere (Fig. 3*C*). For sample with 0 μ W/cm², the peak reflected wavelength was centered at 582 nm; as the UV irradiance increased to 411 μ W/cm², we observed a continuous blueshift by as much as 190 nm to 392 nm. Based on measured reflection spectra, we calculated and mapped the color coordinate in Commission International de I'Eclairage (CIE) space. Detailed calculation is described in *SI Appendix*, Fig. S12 and a supplementary discussion in *SI Appendix*, section S3. Cross-sectional SEM analysis unveiled that the reflection emanates from highly aligned lamellar structure (Fig. 3*D*). Specifically, the average domain spacing (d_{SEM}) decreased from 178 \pm 8.6 to 93.4 \pm 7.0 nm with increasing UV light irradiance, shifting by as much as 85 nm representing a very wide structural tunability. The accessible color range can be further expanded using higher molecular weight BBCP or by swelling the domain using homopolymer additives (48, 51).

We further examined the orientation ordering by imaging cross-sectional microstructure through the entire thickness of both non-cross-linked, and cross-linked lines (*SI Appendix*, Fig. S13 A–H and section S4). The series of SEM images revealed

well-aligned lamellar structures parallel to the substrate throughout the thickness of the sample. The uppermost 15 µm of non-cross-linked line and the uppermost 10 µm of cross-linked line comprise highly ordered lamellae with a 2D orientation order parameter over 0.9 (SI Appendix, Fig. S131). The thickness of the highly ordered top layer corresponds to approximately 80 lamellar periods for non-cross-linked lines and 100 lamellar periods for cross-linked lines (based on the average lamellar d-spacing determined by SEM, Fig. 3D). These number of highly oriented layers for both lines are sufficient to theoretically achieve a reflectivity of 99.9% (detailed calculation is in supplementary discussion in SI Appendix, section S5). Similarly oriented lamella domains were observed near the bottom substrate as well, producing comparable structure color as the top layer (SI Appendix, Fig. S13J). We further analyzed UV-irradiance-dependent cross-sectional profile and lamella structure summarized in SI Appendix, Figs. S14 and S15 and supplementary discussion in SI Appendix, section S4. The printed line width fell in the range of 550 to 580 µm, and the resolution can be potentially increased if using a nozzle as small as 2 µm capable of attaining spatial resolution <3 µm based on literature reports (87, 88). The impact of line width and confinement effect on structure color will be investigated in future work.

To examine the consistency between UV-Vis and SEM, we calculated the domain spacing from peak reflected wavelength using a combination of Bragg's and Snell's law (43, 89).

$$\lambda = 2 \left(n_1 d_1 + n_2 d_2 \right).$$

Here, λ represents the peak reflected wavelength, n_1, n_2 represent the refractive indices of each layer of lamellar, and d₁, d₂ represent the thickness of each layer. In this calculation, the bulk refractive indices of PS (1.586), and PLA (1.465) were used to approximate (52, 62), and $\mathbf{d}_1, \mathbf{d}_2$ were calculated from the total domain size by assuming a volume fraction of $\varphi_{PS}=0.56$ in BBCP (detailed calculation shown in SI Appendix, section S6). This estimation was further substantiated by supplementary Photo-induced Force Microscopy experiments where the measured volume fraction of PS was 0.539 (SI Appendix, Fig. S16). The thus estimated domain spacing from peak reflected wavelength of each line spans 190 to 127 nm as the UV light irradiance increases from 0 to 411 μW/cm², consistent with the observed domain spacing from SEM (Fig. 3E). In addition to the reflection peak shift caused by structural variation, we observed increasing reflection <400 nm at higher irradiance, which we attributed to increased photoinitiator consumption which absorbs below 400 nm (SI Appendix, Fig. S17 and supplementary discussion in *SI Appendix*, section S7).

The stability of the printed lines against extended UV and heat exposure was assessed post printing (SI Appendix, Fig. S18 and section S8). The structure color remained almost unchanged after 3 h of exposure to UV light at a high intensity of 1.5 mW/cm². Therefore, the printed structure color should be able to survive even the harshest printing conditions using our UV-assisted DIW printing method.

Furthermore, the structure color remained stable against thermal annealing as long as the annealing temperature stayed below the glass transition temperature of the uncross-linked PS block (Tg of PLA: 49 °C, PS: 96 °C). Even when annealed at 100 °C for 48 h above the Tg of the PS block, the structure color only slightly whitened (higher saturation values) after such a long heat exposure. This again indicates the high stability of the printed structure color, which we attribute in part to cross-linked structures.

The Molecular Origin of the Evaporation-Driven Assembly and **Structural Color.** We hypothesize that changes in structural color can be attributed to UV light-induced kinetic trapping during evaporative self-assembly. We anticipate that cross-linking "freezesin" the domain size as it increases with concentration during evaporation; BBCPs adopt a more stretched conformation in their self-assembly structure because the removal of solvent induces more block-block contacts, and the polymers tend to minimize these stronger block-block repulsions (60, 62, 90-96). This enhanced segregation increases the BBCP domain spacing so that the structural color undergoes a red-shift during evaporative assembly, which was observed in our experiments (Fig. 4A and SI Appendix, Fig. S11). Cross-linking of one block consequently restricts the relaxation of both blocks, trapping the lamellar structure at a specific domain spacing before it could evolve to its equilibrium structure. This general phenomenon has been demonstrated in several experimental situations, including our recent works showing that length scales of BBCP self-assembly increase with polymer concentration (60, 62, 90, 95, 97, 98). We turn to coarse-grained simulation to demonstrate that, at the molecular level, this predicted self-assembly phenomenon is indeed consistent with the structural color changes that occur in our evaporation-induced process (99).

We recently demonstrated that the order-disorder transition for lamellar BBCP can be modeled using coarse-grained molecular

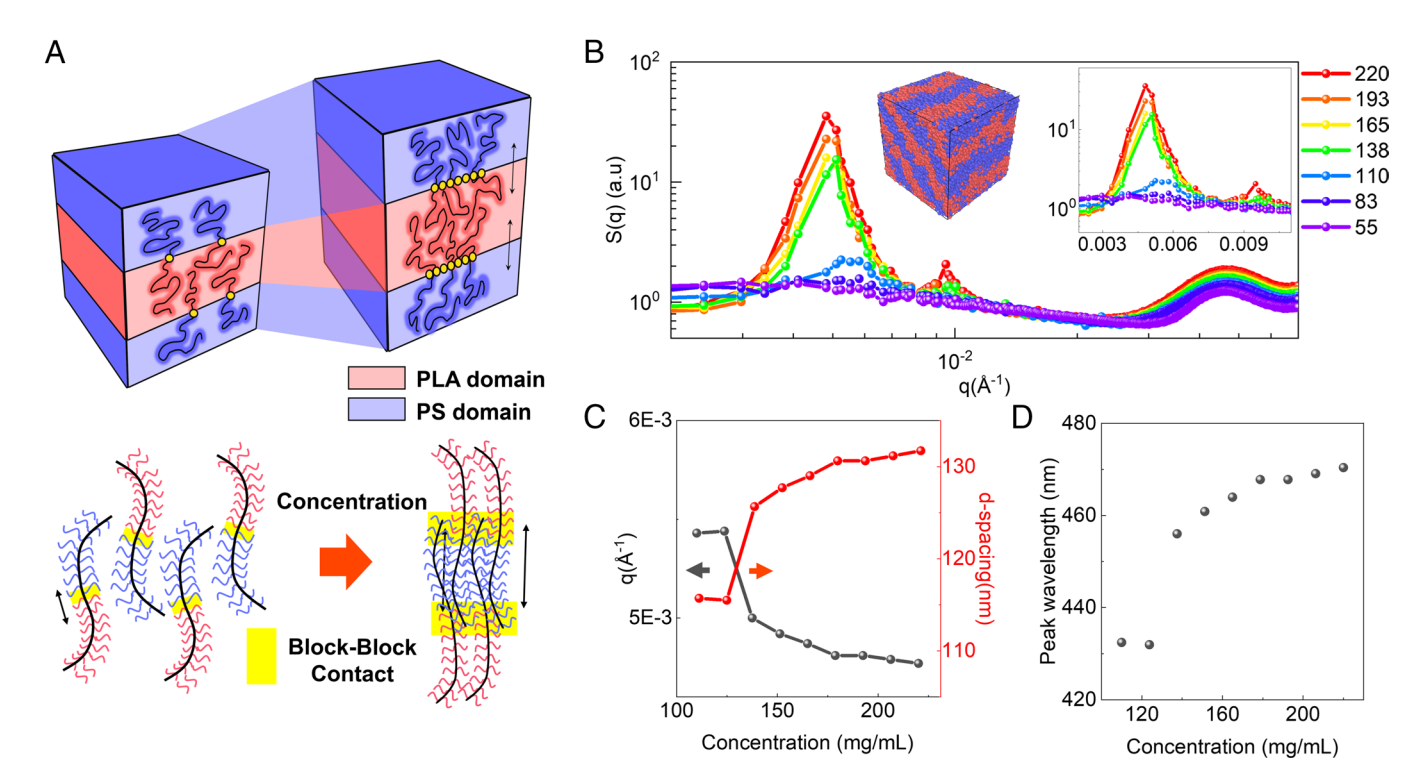


Fig. 4. (A) Schematic of evaporation-driven assembly pathway. When the polymer concentration increases, the BBCPs adopt more stretched conformation due to increased block-block contact by concentration increase. (B) Structure factor S(q) calculated from molecular dynamics simulation at different concentrations. The Inset plots S(q) with a linear scale and shows a representative snapshot of our molecular dynamic simulations at a concentration of 138 mg/mL. (C) The low-q peak positions from S(q) in (B) and corresponding correlation lengths indicating d-spacing of lamellar structure with concentration increase. (D) Estimated UV-vis peak wavelength as a function of solution concentration.

dynamics simulations with a computationally efficient ISC model (62-66), where the coarse-grained beads represent the discretized segments of a BBCP worm-like cylinder model (99). This ISC representation is parameterized directly from bead-spring models at a higher resolution, retaining a minimal description of bottlebrush conformation. This model also accounts for inter-chain interactions through a scaling argument that we describe in our previous works (64, 66). We also now modified the ISC model to account for a concentration-dependent stiffness of the bottlebrush chain, due to increased excluded volume screening between overlapping side chain monomers that renders the bottlebrush more flexible (100–106).

The modified ISC model considers a concentration-dependent extent of overlap, invoking scaling concepts similar to those used to describe semidilute polymer solutions for linear chains (107, 108) and related to other bottlebrush polymer solution scaling

This gives rise to a concentration-dependent persistent length for the ISC model that is due to the non-overlapping bottlebrush "core" near the backbone (109-111). We detail this theory in SI Appendix, Fig. S19 and supplementary discussion in SI Appendix, section S9 and show that it predicts a rapid decrease in the BBCP persistent length with concentration that is consistent with simulations in the literature (112). The concentration-dependent persistent length is integrated into the coarse-grained ISC model, using an overlap concentration $c^* = 55$ mg mL⁻¹that is the key quantity in our scaling model. This modification is necessary to observe the concentration dependence of self-assembled domains, as increased bottlebrush flexibility increases the conformational space available to the chains, and thus their ability to significantly vary their extension (39, 90, 96, 112).

We ran ISC model simulations spanning concentrations from c = 55 to 220 mg mL⁻¹ to observe and compare the concentration-driven self-assembled structure to the experiment, which we quantified using the equilibrium structure factor S(q) (Fig. 4B) described in detail in *SI Appendix*. We use equilibrium simulations to represent experiments, which we assume are in quasi-equilibrium with solvent evaporation occurring much more slowly than the molecular relaxations that set the lamellar dimensions. Upon increasing over the overlap concentration (c*~55 mg mL⁻¹), a low-q peak first emerges at 83 mg mL⁻¹ between 0.003 and 0.005 Å⁻¹ that we attribute to the presence of strong concentration fluctuations. A subsequent ordered peak emerges above 124 mg mL⁻¹ at integer factors of low-q peak, which is indicative of an order-disorder transition that is consistent with both experiment data in our previous work as well as with the dilute ISC model (62, 66) Unlike our previous work, however, the semidilute (i.e., concentration-dependent stiffness) ISC model exhibits a shift of the low-q peak position with increasing concentration (Fig. 4C). The shift of this peak agrees well with experimental trends (60, 62).

We can relate this shift in the low-q peak position q* to the real-space lamellar spacing and the material photonic properties. We first plot in Fig. 4C the lamellar domain spacing d^* as a function of concentration, using the relationship $d^* = 2\pi / q^*$. Plotted d^* ranges from 115 nm to 131 nm, which is in the range of experimental observation (Fig. 3E), demonstrating that the lamellar spacing indeed increases with concentration. A representative simulation snapshot also indicates that BBCPs self-assemble into a lamellar phase (Fig. 4 B, Inset). This is consistent with the experimentally observed change in structural color during evaporation (SI Appendix, Fig. S11). We can further estimate the reflected wavelengths at each d-spacing by matching domain size from SEM to the corresponding UV-vis wavelength in experiment (Fig. 4D). In Fig. 4D, we predict that the reflected wavelength transitions from 432 nm to 470 nm

at concentrations relevant for the experimental data from UV-vis, which ranges from 392 nm to 582 nm (Fig. 3C). This qualitatively captures the experimentally observed trend in solid-state samples, where reflected wavelengths varied from 392 nm to 582 nm, arrested at various stages of the structure evolution by UV cross-linking; we attribute quantitative differences to approximations made in our coarse-graining scheme, in particular the discretization of the bottlebrush wormlike cylinder structure.

Validating Kinetic Trapping Hypothesis by Characterizing Competing Time Scales. Now that we established evaporationdriven assembly pathway, we move on to test another important aspect of our kinetic trapping hypothesis, that photo-cross-linking entraps assembly before the structure reaches equilibrium. This mechanism requires the timescale for the UV-cross-linking to form a gel to be comparable to the timescale for evaporation-driven assembly (i.e., $t_{assembly} \sim t_{gel}$). (Fig. 5A). We estimated $t_{assembly}$ by quantifying the time evolution of hue and intensity for the printed lines through in situ imaging (60) (Fig. 5B). Both values underwent substantial changes after the ink exited the nozzle, with the mean intensity increasing and the hue decreasing, until both values plateaued at approximately 16 s. We thus determined $t_{assembly} \thickapprox 16\,$ s as the time it takes for the color to saturate, given that the color evolution is a manifestation of the lamella domain evolution during evaporative assembly, as established in the previous section.

We take the cross-linking timescale as the time taken to form a gel (t_{gel}), which was estimated based on UV rheological analysis. We show in Fig. 5C the evolution of the dynamic moduli as a function of time before, during, and after UV light exposure at an irradiance of 187 μW/cm² at an angular frequency ω of 5.62 rad/s to illustrate the procedure of determining the cross-linking time $t_{\rm gel}.$ The moduli have been normalized by their equilibrium values, $\overset{"}{G}_{eq}^{'}$ and $\overset{"}{G}_{eq}^{''},$ at times long after UV curing. The accessible range of UV light irradiance was limited, and four different irradiance levels were selected. Experiments were conducted between 60 and 409 μW/cm², closely resembling the estimated irradiance applied by the UV-assisted DIW 3D printer. UV exposure time was set to 15 s, following the estimated assembly time due to evaporation. While there are several ways to define the gel time $t_{\rm gel}$, we choose to define the time since the lamp was first turned on at which the dynamic moduli cross-over to be the gel time, t_{gel}. We discuss alternative metrics and other rheological details in SI Appendix, section S10 (SI Appendix, Fig. S20 and supplementary discussion). The gel time was found to be a little more than $t_{gel} \approx 13\,$ s under the UV light irradiance of $187 \,\mu\text{W/cm}^2$. The same procedure was carried out for the rest of the tested UV light irradiances. For the lower UV light irradiances which do not show the cross-over point within 15 s, linear extrapolation was performed (SI Appendix, Fig. S21). The relation between the t_{gel} and UV light irradiance is represented in Fig. 5D at ω = 5.62 rad/s, exhibiting comparable values with the assembly timescale (t_{assembly} \approx 16 s), consistent with the proposed kinetic trapping mechanism. Further, with increasing UV light irradiance, we observed decreasing t_{gel} suggesting faster cross-link kinetics. To corroborate the UV-rheology, we further estimated the effective cross-link density by equilibrium swelling measurements and Flory-Rehner analysis on printed samples (see detail in Materials and Methods). With increasing UV light irradiance, we found the cross-linking density of the printed line to increase, consistent with faster cross-linking kinetic from rheology measurements (Fig. 5*E*). Taken together, these measurements clearly validate our kinetic

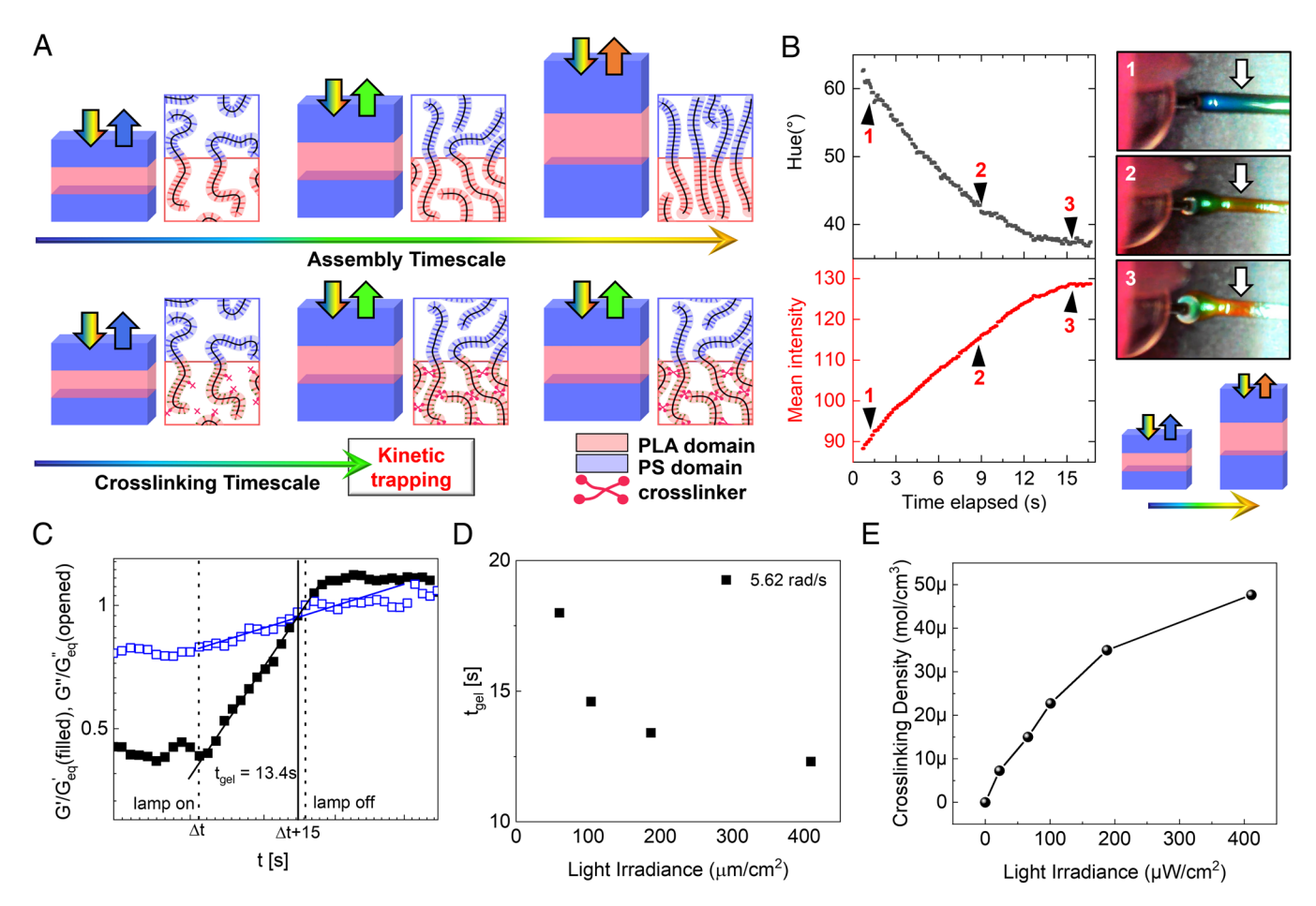


Fig. 5. (A) Schematic depiction of the kinetic trapping mechanism during evaporative assembly: Photo-cross-linking, upon completion, arrests lamella domain expansion before the structure reaches equilibrium. (B) The hue and reflection intensity plotted against elapsed time for printed c-BBCP line. Images are snapshots from the time-lapse video numbered corresponding to the time point indicated by black arrows in the plot. The assembly timescale was estimated based on the point when both hue and reflected intensity values plateau. (C) Time-dependent storage modulus (filled symbol) G' normalized by equilibrium storage modulus G'_{eq} observed at longer time and loss modulus (opened symbol) G' normalized by equilibrium loss modulus G'_{eq} observed at longer time, before, during, and after UV exposure under UV light irradiance of 187 μ W/cm². Gelation time (t_{gel}) was determined from the time when G' and G'' cross-over, which was = 13.4 s determined with respect to the time when turning on the UV lamp. The mutation number during the UV curing was determined to be Mu = 0.073. $t_{\rm gel} = 13.4\,$ s determined with respect to the time when turning on the OV lamp. The mutation number during the OV caring the OV curing (E) The (D) Relation between gelation time $t_{\rm gel}$ and light irradiance (60, 104, 187, and 409 μ W/cm²) at an angular frequency $\omega = 5.62\,$ rad/s during UV curing. (E) The calculated effective cross-linking density of lines printed under various levels of UV light irradiance (0, 22, 62, 101, 188, and 411 μW/cm²).

trapping hypothesis that when the UV cross-linking time is comparable to the assembly timescale, varying light irradiance effectively tunes assembly timescales and entraps the assembled structure further from equilibrium (bluer color) at higher light irradiance due to shorter cross-linking timescale.

We further validated the proposed UV-cross-linking-induced kinetic trapping mechanism by two negative control experiments (SI Appendix, section S11). First, we substantially increased the UV light irradiance to the range of 411 to 1254 µW/cm² and found that the structural color could not be tuned by the irradiance level within this range (SI Appendix, Fig. S22). This shows that if the cross-linking timescale is too short compared to the assembly timescale, assembly was almost instantly frozen and the ability to modulate assembly timescale and therefore structural color is completely lost. Second, we performed printing under otherwise identical conditions but in absence of cross-linking agents (SI Appendix, Fig. S23). Three lines were printed under UV light irradiance of 0, 101 and 411 µW/cm², whose structural colors did not show any difference. These negative control experiments further affirmed that cross-linking at assembly-relevant timescales is critical to structural color modulation.

Gradient Structural Color Printing. Finally, we leverage the interplay of cross-linking kinetics and self-assembly dynamics to attain structural color modulation on the fly. Specifically, we programmed the temporal profile of UV light irradiance to produce prints with color gradients using a single ink material. Shown in Fig. 6A, line 1 was printed by increasing the UV light irradiance from 0 to 188 μ W/cm² to result in orange-to-blue color gradient. Line 2 was produced by reducing UV light irradiance from 101 to $0 \,\mu\text{W/cm}^2$, and then increasing back to $101 \,\mu\text{W/cm}^2$, to yield a line with a gradient of blue to yellow to blue. The as purchased UV light source exhibited significant divergence (SI Appendix, Fig. S24 and section S12), causing low resolution/low sharpness in color transition with a hue slope of 7.52°/mm (SI Appendix, Fig. S24 B and C). To improve the resolution in color transition, we implemented convex lenses (fused silica plano-convex lenses from Thorlabs, Inc.) to collimate the UV light (SI Appendix, Fig. S24D). Using a collimated light source, we obtained a much sharper color transition from orange to blue with an order of magnitude higher hue slope of 72.59°/mm (SI Appendix, Fig. S24 *E* and *F*). We further demonstrated more complex patterns—a chameleon whose color gradually evolved from yellow to blue

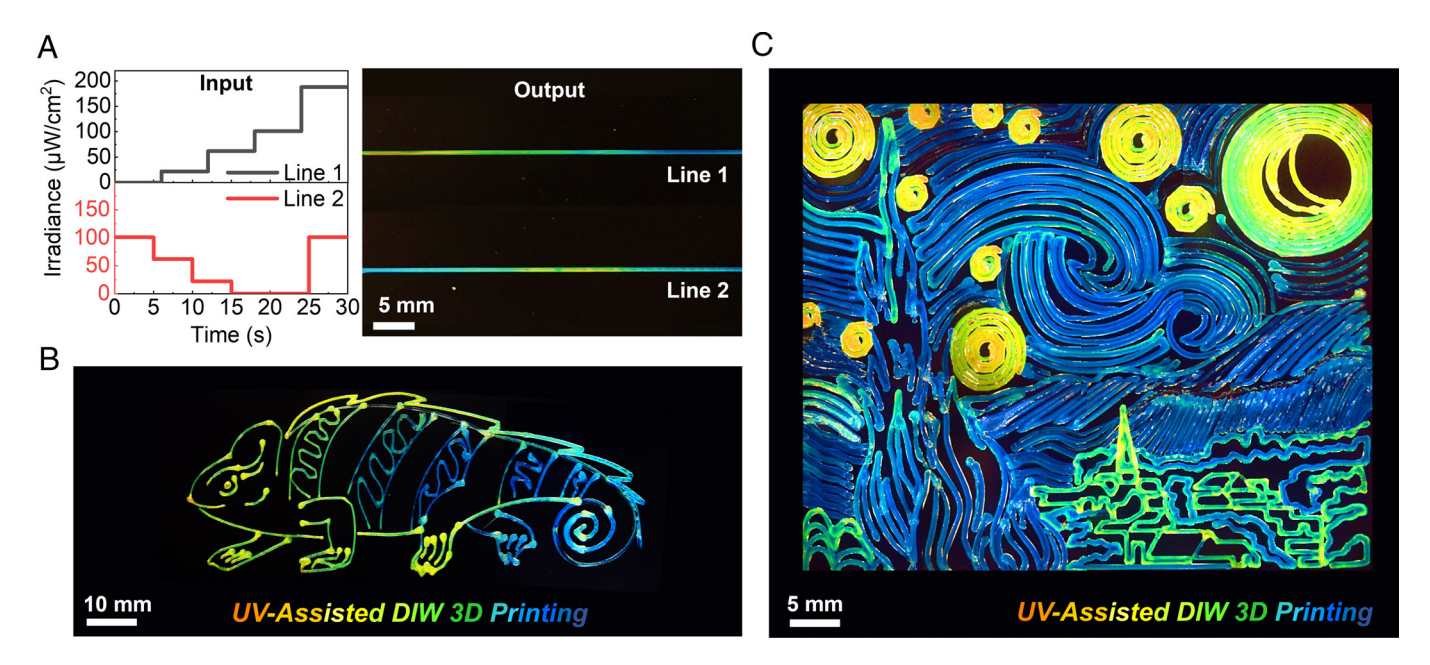


Fig. 6. UV-assisted DIW 3D printing of structural color gradients. (*A*) The digital input of UV light irradiance during printing, and the resulting lines with structural color gradients. (*B* and *C*) Chameleon and Starry Night printed by on-the-fly UV-assisted DIW 3D printing.

from head to tail (Fig. 6*B*), and a mimic of Van Gogh's "The Starry Night" with yellow-to-green moonlight, blue-to-green night sky, and yellow-to-green-to-blue village (Fig. 6*C*).

Conclusion

We present a UV-assisted DIW 3D printing approach capable of on-the-fly modulation of structural color demonstrated using selfassembling PS-b-PLA c-BBCP. This technique enables access to multiple colors during a single printing process using a single ink material, through UV-cross-linking-induced kinetic trapping of evaporative assembly. This approach is enabled by two advances. First, we design and synthesize an allyl-functionalized BBCP which utilizes thiol-ene chemistry for UV cross-linking. Second, we develop a hardware and software framework for UV-assisted DIW 3D printing capable of on-the-fly modulation of crosslinking kinetics by programming UV light irradiance. This approach grants access to structural colors in the visible wavelength spectrum from deep blue (392 nm) to orange (582 nm) by reducing UV light irradiance from 411 to 0 µW/cm². Combining coarse-grained simulation with rheology and in situ structural characterizations, we unveil a cross-linking-induced kinetic trapping mechanism during evaporation assembly. There are two key elements of this assembly mechanism. First, solvent evaporation evolves the structural color of self-assembled lamella from blue to red as the domain spacing increases driven by more block-to-block contact. This insight is enabled by adapting a computationally efficient ISC simulation to model this system. Second, crosslinking is capable of tuning assembly kinetics and structural color only when the cross-linking timescale is comparable to the assembly timescale. Under this condition, increasing cross-linking rate locks in bluer states as the assembly is arrested further from the equilibrium to result in smaller domain spacing. The matching timescale requirement is unveiled by UV rheology combined with in situ imaging and validated by negative control experiments. We finally demonstrate printing of color gradients by modulating UV light irradiance on the fly. Two examples are presented: chameleon and Starry Night with colors spanning blue to green to orange, both produced in a single print using a single ink. Our approach

showcases the power of combining additive manufacturing and non-equilibrium assembly to achieve spatial and temporal control over nanoscale structures and photonic properties.

Materials and Methods

UV-Assisted DIW 3D Printing Ink Preparation. The cross-linkable photonic ink for UV-assisted DIW 3D printing was prepared by dissolving 250 mg of c-BBCP, 40 mg of cross-linker [Pentaerythritol tetrakis(3-mercaptopropionate), Sigma], and 20 mg of photo-initiator (2,2-Dimethoxy-2-phenylacetopheno ne, Sigma) into 1 mL of toluene (anhydrous, 99.8%, Sigma). The c-BBCP ink was capped with aluminum foil to block the light and stirred at room temperature for up to 24 h. Afterward, it was allowed to rest for another 24 h at room temperature without stirring to ensure full recovery. Fabricated ink was loaded into the disposable light block 3 mL amber syringe barrel (Nordson) and capped with a polyethylene piston to avoid evaporation loss during the printing process. The air was removed from the syringe by sealing the end and applying pressure to the piston back before installing the 27-gauge precision stainless steel tip (Nordson).

UV-Assisted DIW 3D Printer and Printing Process. The UV-assisted DIW 3D printer (PCP3_UV) depicted in Fig. 2 and SI Appendix, Fig. S9 constructed based on the modification of the previous PolyChemPrint3. First, we added the UV lamp (OmniCure S2000, Excelitas) and light guide to directly illuminate the nozzle tip. Second, we modified the previous PCP3 software to control multiple tools for simultaneous control. Specifically, we connect the Omnicure UV lamp driver with the main program, thus it can be operated by the main program with other functions (movement, and extrusion). The entire code for the software for PCP3_UV can be found on GitHub (86). The printing of c-BBCP ink was conducted onto the bare silicon wafer or a glass slide that had been cleaned by sonication for 5 min sequentially in toluene, acetone, and isopropanol. The printing z-height was set to 200 µm, and the printing speed and applied pressure were fixed at 100 mm/ min, and 100 kPa, respectively. To perform line printing, an approach was adopted using G-code for linear movement. For complex "chameleon," and "starry night" patterns, we generated motion paths using the Gcodetools plugin for the free vector image software "Inkscape" to make G-code files for drawing. To carry out the structural color printing (simultaneous control of UV light and 3D printing), the UV operation commands were added to the file. Printing "chameleon" requires approximately 10 min, while printing "starry night" patterns takes about 55 min. Following the printing process, all prints are subsequently annealed at 60 °C, for an additional 2 h on the printing bed.

Optical and Structural Characterization. The printed lines or patterns were taken by industrial cameras (PL-D725CU, pixelink) with an apochromatic zoom system (Z16 APO, Leica). All optical measurements were conducted under the diffusive ring lights, and at low magnification (1×). The diffuse reflection spectra were measured using an integrating sphere attachment for a UV-Vis spectroscopy (Varian Cary 5G) located at the Illinois Materials Research Laboratory (MRL). The sample was prepared onto the cleaned glass slide, and corners of prints were cut and delaminated to ensure getting reflection spectra from steady-state regions. The references were taken with respect to a Spectralon standard (100% reflection), and an empty glass slide (0% reflection). The HSB color analysis was done by using ImageJ software package and MATLAB. The structural properties of the sample were analyzed using cross-sectional SEM with a Hitachi S4800 instrument at the Illinois MRL. The sample was prepared onto cleaned silicon substrates. To investigate the vertical direction of the sample, the prints on the silicon substrate were cut perpendicular to the printing direction by inducing controlled crack propagation (a diamond glass scriber was used to create the initial crack). Afterward, the sample was mounted onto a 90-degree angled SEM pin stub, and micrographs were captured using a low accelerating voltage (3 to 5 keV). We used beam current around 10 to 20 nano-Ampere range. The obtained images were subsequently processed using the ImageJ software package to calculate the domain spacing. The calculation of orientation order parameters (S_{2D}) followed three steps: take SEM images parallel to the substrate, generate colorized fiber maps using GTfiber 2.0 software, and generate 2D orientation statistics and parameter. In the protocol generating the colorized fiber maps, lamellae are reduced to a single-pixel width, and an orientation is derived for each of these pixels. The creation of the orientation map involves "filtering" and "skeletonization" steps, and we used auto-optimized values by the software (Gaussian Smoothing: 5 nm, Orientation Smoothing: 15 nm, Diffusion Time: 5 nm, Noise Max Area: 375sq, Fringe Removal: 40 nm) for each step. This procedure outputs both 2D orientation order parameter and a pole figure of 2D orientational order wherein the peak intensity correlates with the population of pixel with a particular orientation. The PiFM imaging was performed using a Molecular Vista PiFM-Raman microscope at the Illinois Materials Research Lab, and the drop-cast samples are prepared onto silicon wafer. More detailed experimental conditions are described in SI Appendix, section S4.

Assembly Time Characterization. The estimation of assembly time was conducted by calculating the changes in hue and reflection intensity using a method that has been previously published (60). The color progression after printing was captured by using in-situ optical microscopy, and the obtained video was analyzed frame-by-frame using an image analysis technique in MATLAB and extracted the hue and intensity changes as a function of time. Related MATLAB code for the calculation can be found in the ref. 60.

Effective Cross-Linking Density Characterization. The effective density of cross-linking was calculated using the Flory-Rehner equation (113).

$$X_c = -\frac{\ln(1-v_2) + v_2 + \chi v_2^2}{V_1(v_2^{\frac{1}{3}} - \frac{v_2}{2})}.$$

- V. Saranathan, S. Narayanan, A. Sandy, E. R. Dufresne, R. O. Prum, Evolution of single gyroid photonic crystals in bird feathers. Proc. Natl. Acad. Sci. U.S.A. 118, 2101357118 (2021).
- V. Saranathan et al., Structure, function, and self-assembly of single network gyroid (14132) photonic crystals in butterfly wing scales. Proc. Natl. Acad. Sci. U.S.A. 107, 11676-11681 (2010), 10.1073/pnas.0909616107.
- D. Gur et al., The mechanism of color change in the neon tetra fish: A light-induced tunable photonic crystal array. Angew. Chem. Int. Ed. Engl. 127, 12603-12607 (2015).
- A. E. Seago, P. Brady, J. P. Vigneron, T. D. Schultz, Gold bugs and beyond: A review of iridescence and structural colour mechanisms in beetles (Coleoptera). J. R. Soc. Interface 6, S165-S184 (2009).
- J. Teyssier, S. V. Saenko, D. Van Der Marel, M. C. Milinkovitch, Photonic crystals cause active colour change in chameleons. Nat. Commun. 6, 6368 (2015).
- A. Gürses, K. Güneş, E. Şahin, "Removal of dyes and pigments from industrial effluents" in Green Chemistry and Water Remediation: Research and Applications, S. K. Sharma, Ed. (Elsevier, 2020), pp. 135-187.
- L. Shang, W. Zhang, K. Xu, Y. Zhao, Bio-inspired intelligent structural color materials. Mater. Horiz. 6, 945-958 (2019).
- Z. Zhang, Z. Chen, L. Shang, Y. Zhao, Structural color materials from natural polymers. Adv. Mater. Technol. 6, 2100296 (2021).
- Y. Zhao, Z. Xie, H. Gu, C. Zhu, Z. Gu, Bio-inspired variable structural color materials. Chem. Soc. Rev. 41, 3297-3317 (2012).

Here, X_c is the effective cross-linking density, V_1 is the molar volume of the solvent at room temperature, χ is Flory–Huggins polymer–solvent interaction parameter, and v_2 is the volume fraction of polymer in swollen sample. The v_2 can be calculated as $v_2 = \frac{w_r}{\rho_r} / \left(\frac{w_r}{\rho_r} + \frac{w_{sol}}{\rho_{sol}} \right)$ where w_r is a weight of unswollen polymer, w_{sol} is a weight of swollen polymer, ρ_r is a density of polymer, and ho_{sol} is a density of solvent. The density of the BBCP ($ho_r=1.13~{
m g/cm^3}$) was estimated based on the calculated volume fraction and the reported density of the bulk homopolymers (PS, and PLA, SI Appendix, section S3). We estimate χ from the reported interaction parameter of PS-toluene ($\chi=0.44$) (114), noting that PS and PLA have similarly good solubility in toluene. The calculated effective cross-linking density of each film printed under the UV light having irradiance of 22, 66, 101, 188, and 411 μW/cm² are 7.25, 15.0, 22.7, 34.9, and 47.7 µmol/cm³, respectively.

UV Rheology Characterization. UV rheology characterization on the ink was performed using an Anton Paar Modular Compact Rheometer 702 in a singledrive model, equipped with a UV curing device OmniCure S2000 accessory (365 nm wavelength). All experiments use a disposable parallel plate geometry with a diameter of 20 mm at a temperature of 5 °C to reduce solvent evaporation. An evaporation hood was used as well to minimize solvent evaporation. Photo-crosslinkable c-BBCP formulations were cured by exposure to UV light for 15 s through a UV-transparent quartz-bottom plate at different light irradiance levels. Before UV curing, the material history related to loading was erased by a pre-shear protocol ($\dot{\gamma} = 25 \text{ 1/s}$) and linear viscoelastic (LVE) spectra are determined by oscillatory shearing at a small strain amplitude ($\gamma_0 = 0.08\,\%$), which was within the moduli-independent regime determined from strain amplitude sweeps. During UV curing, time sweep at a constant oscillatory frequency ($\omega = 5.62 \text{ rad / s}$) and small strain amplitude ($\gamma_0 = 0.08\%$) were applied to monitor the evolution of the dynamic moduli. After the completion of UV curing, as indicated by the plateau in the dynamic moduli, an oscillatory frequency sweep was performed to compare the differences between LVE spectra before and after the curing. All rheological properties were collected via Anton Paar's Rheo Compass software.

Safety Statement. No unexpected or unusually high safety hazards were encountered.

Data, Materials, and Software Availability. All study data are included in the article and/or SI Appendix.

ACKNOWLEDGMENTS. This work was supported by the NSF under Designing Materials to Revolutionize and Engineer our Future (DMREF) award no. DMR-2119172. C.E.S. also acknowledges support from the American Chemical Society (ACS) Petroleum Research Fund under Award Number 61500-ND7.

Author affiliations: ^aDepartment Materials Science and Engineering, University of Illinois at Urbana-Champaign, Urbana, IL 61801; ^bDepartment of Chemical and Biomolecular Engineering, University of Illinois at Urbana-Champaign, Urbana, IL 61801; 'Department of Molecular Science and Engineering, Beckman Institute for Advanced Science and Technology, University of Illinois at Urbana-Champaign, Urbana, IL 61801; and department of Chemistry, University of Illinois at Urbana-Champaign, Urbana, IL 61801

- 10. Z. Wang, C. L. C. Chan, R. M. Parker, S. Vignolini, The limited palette for photonic block-copolymer materials: A historical problem or a practical limitation? Angew. Chem. Int. Ed. Engl. 61, e202117275 (2022).
- 11. Z. Wang, C. L. C. Chan, T. H. Zhao, R. M. Parker, S. Vignolini, Recent advances in block copolymer selfassembly for the fabrication of photonic films and pigments. Adv. Opt. Mater. 9, 2100519 (2021).
- N. Liu et al., Three-dimensional photonic metamaterials at optical frequencies. Nat. Mater. 7, 31-37
- S. H. Nam, J. Park, S. Jeon, Rapid and large-scale fabrication of full color woodpile photonic crystals via interference from a conformal multilevel phase mask. Adv. Funct. Mater. 29, 1904971 (2019).
- Z. Zhang, C. Wang, Q. Wang, Y. Zhao, L. Shang, Cholesteric cellulose liquid crystal ink for three-dimensional structural coloration. Proc. Natl. Acad. Sci. U.S.A. 119, 2204113119 (2022).
- K. George et al., 3D printing of responsive chiral photonic nanostructures. Proc. Natl. Acad. Sci. U.S.A. 120, e2220032120 (2023).
- C. L. C. Chan et al., 3D printing of liquid crystalline hydroxypropyl cellulose–Toward tunable and sustainable volumetric photonic structures. Adv. Funct. Mater. 32, 2108566 (2022).
- A. F. Demirörs et al., Three-dimensional printing of photonic colloidal glasses into objects with isotropic structural color. Nat. Commun. 13, 4397 (2022).
- J. Liao et al., 3D-printable colloidal photonic crystals. Mater. Today 56, 29-41 (2022).
- Y. Zhang et al., Continuous resin refilling and hydrogen bond synergistically assisted 3D structural color printing. Nat. Commun. 13, 7095 (2022).

- 20. A. Patil et al., Structural color production in melanin-based disordered colloidal nanoparticle assemblies in spherical confinement. Adv. Opt. Mater. 10, 2102162 (2022).
- A. Patil et al., Modeling structural colors from disordered one-component colloidal nanoparticlebased supraballs using combined experimental and simulation techniques. ACS Mater. Lett. 4, 1848-1854 (2022).
- C. M. Heil et al., Mechanism of structural colors in binary mixtures of nanoparticle-based supraballs. Sci. Adv. 9, eadf2859 (2023).
- B. M. Boyle, T. A. French, R. M. Pearson, B. G. McCarthy, G. M. Miyake, Structural color for additive manufacturing: 3D-printed photonic crystals from block copolymers. ACS Nano 11, 3052–3058 (2017)
- T. H. Park et al., Block copolymer structural color strain sensor. NPG Asia Mater. 10, 328-339 (2018).
- H. S. Lim, J. H. Lee, J. J. Walish, E. L. Thomas, Dynamic swelling of tunable full-color block copolymer 25. photonic gels via counterion exchange. ACS Nano 6, 8933-8939 (2012).
- H. S. Kang et al., Printable and rewritable full block copolymer structural color. Adv. Mater. 29, 1700084 (2017).
- Y. Mai, A. Eisenberg, Self-assembly of block copolymers. Chem. Soc. Rev. 41, 5969-5985 (2012).
- F. S. Bates, G. H. Fredrickson, Block copolymer thermodynamics: Theory and experiment. Annu. Rev. 28 Phys. Chem. 41, 525-557 (1990).
- C. Zhang et al., Emergence of hexagonally close-packed spheres in linear block copolymer melts. J. Am. Chem. Soc. 143, 14106-14114 (2021).
- S. M. Barbon et al., Architecture effects in complex spherical assemblies of (AB)n-type block copolymers. ACS Macro Lett. 9, 1745-1752 (2020).
- S. Lee, M. J. Bluemle, F. S. Bates, Discovery of a Frank-Kaspers sigma phase in sphere-forming block copolymer melts. Science 330, 349-353 (2010).
- L. Xiang et al., Block copolymer self-assembly directed synthesis of porous materials with ordered bicontinuous structures and their potential applications. Adv. Mater. 35, e2207684 (2023). 32.
- V. Choo, P. W. Majewski, M. Fukuto, C. O. Osuji, K. G. Yager, Pathway-engineering for highly-aligned block copolymer arrays. *Nanoscale* **10**, 416–427 (2018).
- $\hbox{C. Lee \it et al.}, \hbox{\it Effects of labile mesogens on the morphology of liquid crystalline block copolymers in}$ 34 thin films. Macromolecules 54, 3223-3231 (2021).
- $S.\ Nian\ et\ al., Self-assembly\ of\ flexible\ linear-semiflexible\ bottlebrush-flexible\ linear\ triblock$ copolymers. Macromolecules 54, 9361-9371 (2021).
- Z. Guo et al., Discovering ordered phases of block copolymers: New results from a generic fourierspace approach. Phys. Rev. Lett. 101, 028301 (2008).
- E. B. Zhulina, S. S. Sheiko, A. V. Dobrynin, O. V. Borisov, Microphase segregation in the melts of bottlebrush block copolymers. Macromolecules 53, 2582-2593 (2020).
- R. Liang et al., Hierarchically engineered nanostructures from compositionally anisotropic molecular building blocks. *Nat. Mater.* 21, 1434–1440 (2022).
- M. Chen et al., Chain flexibility effects on the self-assembly of diblock copolymer in thin films. Macromolecules 56, 1704-1712 (2023).
- C. U. Lee, R. Khalifehzadeh, B. Ratner, A. J. Boydston, Facile synthesis of fluorine-substituted polylactides and their amphiphilic block copolymers. *Macromolecules* **51**, 1280–1289 (2018). E. C. Davidson *et al.*, Impact of helical chain shape in sequence-defined polymers on polypeptoid block copolymer self-assembly. *Macromolecules* **51**, 2089–2098 (2018).
- D. P. Song et al., Photonic resins: Designing optical appearance via block copolymer self-assembly. Macromolecules 51, 2395-2400 (2018).
- A. L. Liberman-Martin, C. K. Chu, R. H. Grubbs, Application of bottlebrush block copolymers as photonic crystals. Macromol. Rapid Commun. 38, 1700058 (2017).
- H. S. Kang et al., 3D touchless multiorder reflection structural color sensing display. Sci. Adv. 6,
- Y. Kang, J. J. Walish, T. Gorishnyy, E. L. Thomas, Broad-wavelength-range chemically tunable blockcopolymer photonic gels. *Nat. Mater.* **6**, 957–960 (2007).
- T. Pan et al., Materials design of highly branched bottlebrush polymers at the intersection of modeling, synthesis, processing, and characterization. Chem. Mater. 34, 1990-2024 (2022).
- G. M. Miyake, V. A. Piunova, R. A. Weitekamp, R. H. Grubbs, Precisely tunable photonic crystals from rapidly self-assembling brush block copolymer blends. *Angew. Chem. Int. Ed. Engl.* **51**, 11246-11248 (2012).
- B. R. Sveinbjörnsson et al., Rapid self-assembly of brush block copolymers to photonic crystals. Proc. Natl. Acad. Sci. U.S.A. 109, 14332–14336 (2012).
- C. G. Chae et al., Experimental formulation of photonic crystal properties for hierarchically self-assembled POSS-bottlebrush block copolymers. Macromolecules 51, 3458-3466 (2018).
- Y. G. Yu \textit{et al.}, Precise synthesis of bottlebrush block copolymers from ω -end-norbornyl polystyrene and poly(4-tert-butoxystyrene) via Living anionic polymerization and ring-opening metathesis polymerization. Macromolecules 51, 447-455 (2018).
- G. M. Miyake, R. A. Weitekamp, V. A. Piunova, R. H. Grubbs, Synthesis of isocyanate-based brush block copolymers and their rapid self-assembly to infrared-reflecting photonic crystals. J. Am. Chem. Soc. 134, 14249-14254 (2012).
- B. B. Patel et al., Rapid, interface-driven domain orientation in bottlebrush diblock copolymer films during thermal annealing. Soft Matter 18, 1666-1677 (2022).
- H. Mei et al., Entropy and enthalpy mediated segregation of bottlebrush copolymers to interfaces. Macromolecules **52**, 8910–8922 (2019).
- $H.\ Liang, Z.\ Cao, Z.\ Wang, S.\ S.\ Sheiko, A.\ V.\ Dobrynin, Combs \ and \ bottlebrushes \ in \ a \ melt.$ 54. Macromolecules 50, 3430-3437 (2017).
- T. H. Zhao et al., Angular-independent photonic pigments via the controlled micellization of amphiphilic bottlebrush block copolymers. *Adv. Mater.* **32**, e2002681 (2020).

 56. D. P. Song, T. H. Zhao, G. Guidetti, S. Vignolini, R. M. Parker, Hierarchical photonic pigments via the
- confined self-assembly of bottlebrush block copolymers. ACS Nano 13, 1764-1771 (2019).
- X. Chen, D. P. Song, Y. Li, Precisely tunable photonic pigments via interfacial self-assembly of bottlebrush block copolymer binary blends. Macromolecules 55, 7438-7445 (2022).
- M. A. Wade et al., Color, structure, and rheology of a diblock bottlebrush copolymer solution. Soft Matter 16, 4919-4931 (2020).
- X. Li et al., Supersoft elastic bottlebrush microspheres with stimuli-responsive color-changing properties in brine. Langmuir 37, 6744-6753 (2021).
- B. B. Patel et al., Tunable structural color of bottlebrush block copolymers through direct-write 3D printing from solution. Sci. Adv. 6, 7202-7212 (2020).
- B. B. Patel et al., PolyChemPrint: A hardware and software framework for benchtop additive manufacturing of functional polymeric materials. J. Polym. Sci. 59, 2468-2478 (2021).

- 62. B. B. Patel et al., Concentration-driven self-assembly of PS-b-PLA bottlebrush diblock copolymers in solution. ACS Polym. Au 2, 232-244 (2022).
- S. Dutta, C. E. Sing, Two stretching regimes in the elasticity of bottlebrush polymers. *Macromolecules* **53**, 6946-6955 (2020).
- T. Pan, S. Dutta, C. E. Sing, Interaction potential for coarse-grained models of bottlebrush polymers. J. Chem. Phys. 156, 014903 (2022).
- 65. S. Dutta, T. Pan, C. E. Sing, Bridging simulation length scales of bottlebrush polymers using a wormlike cylinder model. Macromolecules 52, 4858-4874 (2019).
- T. Pan et al., Implicit side-chain model and experimental characterization of bottlebrush block copolymer solution assembly. *Macromolecules* **54**, 3620–3633 (2021). E. Blasco, M. B. Sims, A. S. Goldmann, B. S. Sumerlin, C. Barner-Kowollik, 50th anniversary
- perspective: Polymer functionalization. Macromolecules 50, 5215-5252 (2017).
- A. S. Goldmann, M. Glassner, A. J. Inglis, C. Barner-Kowollik, Post-functionalization of polymers via orthogonal ligation chemistry. Macromol. Rapid Commun. 34, 810-849 (2013).
- D. Zhou, L. W. Zhu, B. H. Wu, Z. K. Xu, L. S. Wan, End-functionalized polymers by controlled/living radical polymerizations: Synthesis and applications. Polym. Chem. 13, 300-358 (2022).
- D. J. Lunn, E. H. Discekici, J. Read de Alaniz, W. R. Gutekunst, C. J. Hawker, Established and emerging strategies for polymer chain-end modification. J. Polym. Sci. A Polym. Chem. 55, 2903-2914
- 71. J. Tellers et al., Dynamic cross-linking of polyethylene via sextuple hydrogen bonding array. Macromolecules 51, 7680-7691 (2018).
- D. H. Howe, R. M. McDaniel, A. J. D. Magenau, From click chemistry to cross-coupling: Designer polymers from one efficient reaction. Macromolecules 50, 8010-8018 (2017).
- C. G. Chae et al., End-capping reaction of living anionic poly(benzyl methacrylate) with a pentafluorophenyl ester for a norbornenyl-ω-end macromonomer with a long flexible spacer: Advantage in the well-controlled synthesis of ultrahigh-molecular-weight bottlebrush polymers. Macromolecules 52, 4828-4838 (2019).
- C. Chen, C. G. Wang, W. Guan, A. Goto, A photo-selective chain-end modification of polyacrylateiodide and its application in patterned polymer brush synthesis. *Polym. Chem.* **10**, 5913–5919
- S. J. Bailey et al., Norbornadiene chain-end functional polymers as stable, readily available precursors to cyclopentadiene derivatives. Macromolecules 53, 4917-4924 (2020).
- K. Fuchise, K. Sato, M. Igarashi, Precise synthesis of linear polysiloxanes end-functionalized with alkynylsilyl groups by organocatalytic ring-opening polymerization of cyclotrisiloxanes. Macromolecules 54, 5765-5773 (2021).
- S. Agar, E. Baysak, G. Hizal, U. Tunca, H. Durmaz, An emerging post-polymerization modification technique: The promise of thiol-para-fluoro click reaction. J. Polym. Sci. A Polym. Chem. 56, 1181-1198 (2018).
- J. Köhler, H. Keul, M. Möller, Post-polymerization functionalization of linear polyglycidol with
- diethyl vinylphosphonate. *Chem. Commun.* **47**, 8148–8150 (2011).
 D. J. Walsh, M. G. Hyatt, S. A. Miller, D. Guironnet, Recent trends in catalytic polymerizations. *ACS Catal.* **9**, 11153–11188 (2019).
- D. J. Walsh, M. A. Wade, S. A. Rogers, D. Guironnet, Challenges of size-exclusion chromatography for the analysis of bottlebrush polymers. Macromolecules 53, 8610-8620 (2020).
- H. Mei et al., Rapid processing of bottlebrush coatings through UV-induced cross-linking. ACS Macro Lett. 9, 1135-1142 (2020).
- F. Biedermann et al., Postpolymerization modification of hydroxyl-functionalized polymers withisocyanates. Macromolecules 44, 4828-4835 (2011).
- B. H. Northrop, R. N. Coffey, Thiol-ene click chemistry: Computational and kinetic analysis of the influence of alkene functionality. J. Am. Chem. Soc. 134, 13804-13817 (2012).
- Y. Adeli, F. Owusu, F. A. Nüesch, D. M. Opris, On-demand cross-linkable bottlebrush polymers for voltage-driven artificial muscles. ACS Appl. Mater. Interfaces 15, 20410-20420 (2023).
- J. A. Van Hensbergen, R. P. Burford, A. B. Lowe, Post-functionalization of a ROMP polymer backbone via radical thiol-ene coupling chemistry. J. Polym. Sci. A Polym. Chem. 51, 487-492 (2013).
- B. B. Patel, PolyChemPrint3 software (2021). https://github.com/BijalBPatel/PolyChemPrint3.
- Y. Liu *et al.*, Meniscus-guided 3D microprinting of pure metal-organic frameworks with high gas-uptake performance. *ACS Appl. Mater. Interfaces* **14**, 7184–7191 (2022).
- J. H. Kim et al., Meniscus-guided micro-printing of prussian blue for smart electrochromic display. Adv. Sci. 10, 2205588 (2023).
- A. C. Edrington et al., Polymer-based photonic crystals. Adv. Mater. 13, 421-425 (2001).
- Y. W. Chiang et al., Large-area block copolymer photonic gel films with solvent-evaporation-induced red- and blue-shift reflective bands. Macromolecules 48, 4004-4011 (2015).
- E. Helfand, Y. Tagami, Theory of the interface between immiscible polymers. II. J. Chem. Phys. 56, 3592-3601 (1972).
- S. P. Paradiso, K. T. Delaney, C. J. García-Cervera, H. D. Ceniceros, G. H. Fredrickson, Block copolymer self assembly during rapid solvent evaporation: Insights into cylinder growth and stability. ACS Macro Lett. 3, 16-20 (2014).
- A. L. Patterson et al., Sequence effects on block copolymer self-assembly through tuning chain conformation and segregation strength utilizing sequence-defined polypeptoids. Macromolecules **52**, 1277-1286 (2019).
- L. Leibler, Theory of microphase separation in block copolymers. Macromolecules 13, 1602-1617 (1980).
- Y. Matsushita et al., Molecular weight dependence of lamellar domain spacing of diblock copolymers in bulk. Macromolecules 23, 4313-4316 (1990).
- Y. Jiang, W. Y. Zhang, J. Z. Y. Chen, Dependence of the disorder-lamellar stability boundary of a melt of asymmetric wormlike AB diblock copolymers on the chain rigidity. Phys. Rev. E Stat. Nonlin Soft Matter Phys. 84, 041803 (2011).
- J. Zhang et al., Lamellar diblock copolymer thin films during solvent vapor annealing studied by gisaxs: Different behavior of parallel and perpendicular lamellae. Macromolecules 47, 5711-5718
- M. Shibayama, T. Hashimoto, H. Hasegawa, H. Kawai, Ordered structure in block polymer solutions. 3. Concentration dependence of microdomains in nonselective solvents. Macromolecules 16,
- E. Mohammadi, S. Y. Joshi, S. A. Deshmukh, A review of computational studies of bottlebrush polymers. Comput. Mater. Sci. 199, 110720 (2021).
- 100. K. Fischer, M. Schmidt, Solvent-induced length variation of cylindrical brushes. Macromol. Rapid Commun. 22, 787-791 (2001).

- 101. M. S. Rocha et al., Force and scale dependence of the elasticity of self-assembled DNA bottle brushes. Macromolecules 51, 204-212 (2018).
- 102. T. M. Birshtein, O. V. Borisov, Y. B. Zhulina, A. R. Khokhlov, T. A. Yurasova, Conformations of comb-like macromolecules. Polym. Sci. U.S.S.R. 29, 1293-1300 (1987).
- 103. Y. Nakamura, T. Norisuye, Backbone stiffness of comb-branched polymers. *Polym. J.* 33, 874-878
- 104. I. M. Storm *et al.*, Loss of bottlebrush stiffness due to free polymers. *Soft Matter* **12**, 8004–8014(2016). 105. J. Paturej, T. Kreer, Hierarchical excluded volume screening in solutions of bottlebrush polymers.
- Soft Matter 13, 8534-8541 (2017).
- D. F. Sunday et al., Concentration dependence of the size and symmetry of a bottlebrush polymer in a good solvent. *Macromolecules* 53, 7132–7140 (2020).
 M. Rubinstein, R. H. Colby, *Polymer Physics* (Oxford University Press, 2003).
- 108. P.-G. de Gennes, Scaling Concepts in Polymer Physics (Cornell University Press, 1979).

- 109. E. B. Zhulina, S. S. Sheiko, O. V. Borisov, Solution and melts of barbwire bottlebrushes: Hierarchical structure and scale-dependent elasticity. Macromolecules 52, 1671-1684 (2019).
- 110. G. Yang et al., Scaling laws for polymer chains grafted onto nanoparticles. Macromol. Chem. Phys. **219**, 1700417 (2018).
- 111. M. Daoud, J. P. Cotton, Star shaped polymers: A model for the conformation and its concentration dependence. J. Phys. Paris 43, 531-538 (1982).
- J.J. Kang et al., Rigid-to-flexible transition in a molecular brush in a good solvent at a semidilute concentration. *Langmuir* 38, 5226-5236 (2022).
 P.J. Flory, J. Rehner, Statistical mechanics of cross-linked polymer networks II. Swelling. *J. Chem.*
- P. J. Flory, J. Refinet, Statistical mechanics of cross-mixed polymer methods in Chemistry Phys. 11, 521–526 (1943).
 H.-S. Tseng, D. R. Lloyd, T. C. Ward, Interaction parameters of polystyrene-polyisoprene-toluene systems at 45°c from gel permeation chromatography. *J. Polym. Sci. B Polym. Phys.* 25, 325–337